Solid State Communications 394 (2024) 115700

Contents lists available at ScienceDirect

Solid State Communications

journal homepage: www.elsevier.com/locate/ssc

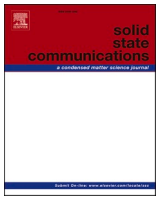

Thermal conductivity reduction and crystal properties evolution in iron silicides induced by doping

Sopheap Sam [a], Kosuke Yamazaki [b], Hiroshi Nakatsugawa [b,*]

[a] National Institute for Materials Science, Tsukuba, Ibaraki, 305-0044, Japan
[b] Yokohama National University, Yokohama, 240-8501, Japan

ARTICLE INFO

Communicated by: Francois Peeters

Keywords:
Silicides
Thermal conductivity
Crystal properties
Lattice softening
Phonon scattering

ABSTRACT

Understanding the thermal transport behaviors in the crystal lattice is important for designing semiconducting materials in thermal management. In this work, we investigate the mechanism of the decrease in thermal properties of β-$FeSi_2$ when Co dopant is introduced to the host crystal. The crystallite size decreases as Co doping increases from 0 to 5 %. The micro-strain and stress increase with increasing doping levels. The decrease in crystallite size and increase in micro-strain/stress indicate the origin of phonons scattering and lattice softening, leading to the reduction in thermal conductivity. This study provides insights into the correlation between the crystal properties evolution and thermal transport in metal silicide compounds which could be useful in thermal-to-energy conversion applications.

1. Introduction

It has been a challenge to understand thermal transport behaviors in the crystal lattice, especially when dopants are introduced to the host crystal. Understanding thermal transport phenomena is essential to designing semiconducting materials in various electronic applications. Especially, thermoelectric (TE) generators that can directly convert thermal energy to electricity have gained attention in energy conversion technology and thermal management in electronics [1,2]. The TE conversion efficiency of the device is mainly proportional to material performance which is called the dimensionless figure of merit (*ZT*). The *ZT* value is equal to $ZT = S^2T\rho^{-1}\kappa^{-1}$, where *S* is the Seebeck coefficient, *T* is temperature, ρ is electrical resistivity, κ is the total thermal conductivity contributed by electronic and lattice thermal conductivity ($\kappa = \kappa_e + \kappa_l$) and the term $S^2\rho^{-1}$ is usually called the power factor (*PF*) [3]. The improvement of *ZT* can be obtained by both increasing the power factor and reducing thermal conductivity. The reduction in thermal conductivity remains the main challenge as it may also affect the power factor. Therefore, understanding the mechanism of thermal conductivity reduction needs to be further discussed in-depth.

Semiconducting iron silicide (β-$FeSi_2$) compounds have attracted attention in TE applications operating at high temperatures due to their ability to withstand oxidation and exhibit good thermal stability. The reduction of thermal conductivity of the materials can be obtained by nanostructuring techniques [4] and doping with heavier elements [5]. Previous studies found the addition of dopants such as Ge [5], Ru [6], Mn [7,8], Ir [9], Ni [10,11], Os [12], and Co [13–16], lead to decreases in thermal conductivity, suggesting that those dopants act as heavy elements and scatter the phonons in the β-$FeSi_2$ system. In other materials, it was pointed out that dopant also induces internal strain, resulting in lattice softening and phonon scattering in PbTe [17] and half Heusler compounds [18]. The phonons travel fast without dopant, resulting in high thermal conductivity. When dopant is introduced to the host crystal, it may induce tensile strain and compressive strain, where the speed of phonon can be slowed down (lattice softening) and relaxation time will be shorter (phonon scattering), resulting in a reduction in lattice thermal conductivity.

The Co element is considered one of the effective dopants to improve the TE performance of the β-$FeSi_2$ system [13–16,19], where it helps to improve the power factor and reduce the thermal conductivity. However, the mechanism of strain-induced effect on the thermal conductivity in the Co-doped β-$FeSi_2$ system has not been investigated. In this work, we investigate in detail the effect of strain induced by Co on β-$FeSi_2$ and its relations with the thermal conductivity. In addition, the crystal quality (crystallite size) of Co-doped β-$FeSi_2$ is also reported. It is expected that the crystallite size should also have an impact on the thermal properties. The compounds of $Fe_{1-x}Co_xSi_2$ (where *x* ranges from 0 to 0.05) were chosen for the analysis because the optimum doping

* Corresponding author.
E-mail address: nakatsugawa-hiroshi-dx@ynu.ac.jp (H. Nakatsugawa).

https://doi.org/10.1016/j.ssc.2024.115700
Received 21 July 2024; Received in revised form 4 September 2024; Accepted 17 September 2024
Available online 19 September 2024

levels for improving TE performance are within this range [19–24].

2. Experimental methods

The raw elements of Fe grain (99.9 % up), Si grain (99.999 %), and Co powder (99 % up) were weighed (total mass of 20g) following the composition range of $Fe_{1-x}Co_xSi_2$ ($0 \leq x \leq 0.05$). To make the ingots, the mixtures of raw elements were arc-melted in an Ar atmosphere under 10^{-3} Pa. The ingots were flipped and remelted three times to ensure homogeneity. The obtained ingots were sliced into appropriate pieces (7mm × 7mm × 1.5 mm) by a numerical control wire-cutting machine (EC-3025, Makino) for thermal conductivity measurement. The arc-melted ingots were in the metallic phases (α-Fe_2Si_5 + ε-FeSi). Therefore, the heat treatments at 1423K for 3h and followed by 1113K for 20h were applied to transform the metallic phases into the semiconducting phase (β-$FeSi_2$) [25]. It should be noted the first step of heat treatment is to further homogenize the distribution of the material, while the second step is for the transformation of semiconducting β-$FeSi_2$.

The total thermal conductivity (κ_T) was evaluated with the help of a power efficiency measurement system (PEM2, ULVAC, Inc). The κ_T can be evaluated by the following equation:

$$\kappa_T = \frac{qA}{\Delta T}\frac{1}{\frac{LW}{t}} \quad (1)$$

Where q is the heat flow density through the copper block, A is the cross-section area of the copper block, ΔT is the temperature difference of the sample, and L, W, and t are the sample's lengths, width, and thickness, respectively. PEM-2 can evaluate the q from the known thermal conductivity values of copper blocks. The value of q was calculated in the software. Therefore, κ_T can be calculated from the above equation. In addition, the sample has carbon sheets inserted at the top and bottom to ensure good thermal contact with the PEM-2 measurement. The electronic thermal conductivity (κ_E) was calculated from the Wiedemann–Franz law using the values of electrical resistivity (ρ) and the Seebeck coefficient (S) measured by the ResiTest8300 apparatus (TOYO Co.). The details of κ_E calculation will be discussed in the next section: Results and discussion. The lattice thermal conductivity (κ_L) is the subtraction of total thermal conductivity with electronic thermal conductivity ($\kappa_L = \kappa_T - \kappa_E$). The microstructures were characterized by a scanning electron microscope (SEM, VE-8800 KEYENCE). The Rietveld refinement method was used to calculate the crystal parameters from the X-ray diffraction (XRD) data measured by the X-ray diffractometer equipped with Cu Kα radiation (High-resolution SmartLab, RIGAKU). The standard crystal data were referred to the Inorganic Crystal Structure Database (ICSD), where code #5257-ICSD [26], #41997-ICSD [27], and #9119-ICSD [28] were used for α-phase, ε-phase, and β-phase, respectively. The full width at half maximum (FWHM) values obtained from Rietveld refinement were used to evaluate crystalline quality such as the crystallite size and micro-strain.

3. Results and discussion

The thermal conductivity of $Fe_{1-x}Co_xSi_2$ with x dependence at room temperature is plotted in Fig. 1. The trend indicates that the lattice thermal conductivity (κ_L) decreases from 7.67 to 5.13 $Wm^{-1}K^{-1}$ as x increases from 0 to 0.05. In contrast to κ_L, the value of the electronic thermal conductivity (κ_E) is quite small, and it increases from 7.57 × 10^{-5} to 4.86 × 10^{-2} $Wm^{-1}K^{-1}$ as x increases from 0 to 0.05, respectively. The electronic thermal conductivity (κ_E) is calculated by Wiedemann–Franz law: $\kappa_E = L_0T/\rho$, where L_0 is Lorenz number, T is temperature, and ρ is the electrical resistivity. This implies that ρ is inversely proportional to κ_E. The ρ values are measured by four probes method and the results are plotted in Fig. S1 (Supporting Information). It is shown that the ρ of the non-doped samples is about two orders of magnitude higher than that of the Co-doped samples. Therefore, since

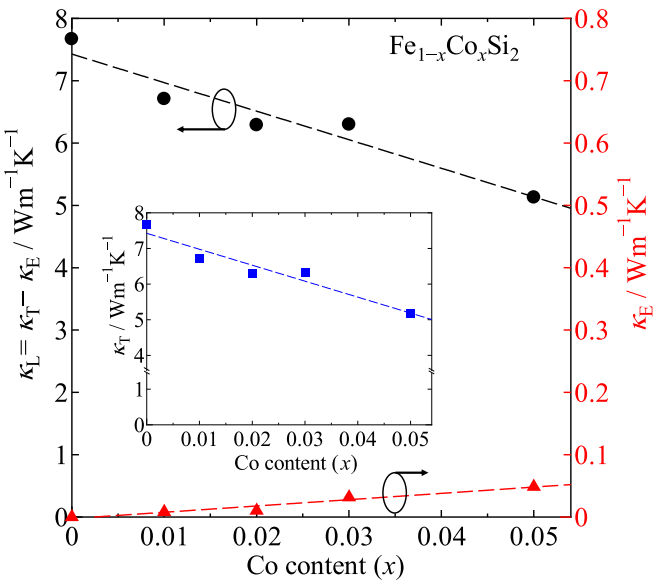

Fig. 1. The thermal conductivity of $Fe_{1-x}Co_xSi_2$ with x dependence at 300 K from our previous work in Ref. [13]. The lattice thermal conductivity is the subtraction of total thermal conductivity with electronic thermal conductivity ($\kappa_L = \kappa_T - \kappa_E$) plotted on the left axis. The electronic part (κ_E) is plotted on the right axis. The inset plots the total thermal conductivity (κ_T).

the ρ is inversely proportional to κ_E, the κ_E of the non-doped sample is lower than that of Co-doped samples. Next, the L_0 is calculated from the Seebeck coefficient (S). In the case of acoustic phonon scattering (scattering factor $r = -1/2$), L_0 is defined by Ref. [29]:

$$L_0 = \left(\frac{k_B}{e}\right)^2 \left[\frac{\left(r+\frac{7}{2}\right)F_{r+\frac{5}{2}}(\eta)}{\left(r+\frac{3}{2}\right)F_{r+\frac{1}{2}}(\eta)} - \left\{\frac{\left(r+\frac{5}{2}\right)F_{r+\frac{3}{2}}(\eta)}{\left(r+\frac{3}{2}\right)F_{r+\frac{1}{2}}(\eta)}\right\}^2\right] \quad (2)$$

where $F_n(\eta) = \int_0^\infty \frac{\chi^n}{1+e^{\chi-\eta}}d\chi$, $\chi = \frac{E}{k_BT}$, $\eta = \frac{E_F}{k_BT}$, and E_F is the Fermi energy. The relationship between η and the Seebeck coefficient (S) is expressed by:

$$S = \pm\frac{k_B}{e}\left(2\frac{F_1(\eta)}{F_0(\eta)} - \eta\right) \quad (3)$$

From **Equation (3)**, η can be determined by fitting the experimental value of absolute $|S|$ at room temperature. Thus, L_0 can be consequently evaluated from **Equation (2)**. The measured ρ is plotted in Fig. S1 and the calculated L_0 and the measured S are plotted in Fig. S2 (Supporting Information). Then, κ_E can be calculated by using the Wiedemann–Franz law.

However, compared to κ_L, the value of κ_E is so small and negligible. As shown in the inset of Fig. 1, the total thermal conductivity (κ_T) has the same trends as κ_L and it decreases from 7.67 to 5.18 $Wm^{-1}K^{-1}$ with increasing x from 0 to 0.05, indicating that κ_L is dominant to κ_T. These thermal conductivity values of arc-melted samples are larger than those prepared by spark plasma sintering (3.95 $Wm^{-1}K^{-1}$) [19], which is probably due to the difference in crystallite sizes. Since our fabrication process of all samples is the same, the reduction of total thermal conductivity (κ_T) should be mainly caused by Co substitution, where the phonons scattering or lattice softening should happen in the crystal lattice. In addition, since the κ_T of the non-doped sample is higher than that of the Co-doped samples, it must also have a larger crystallite size and less phonon scattering. Then, we further investigate the mechanism of how the Co atom influences the host β-$FeSi_2$ crystal.

The variation of microstructure in non-doped β-$FeSi_2$ is shown in

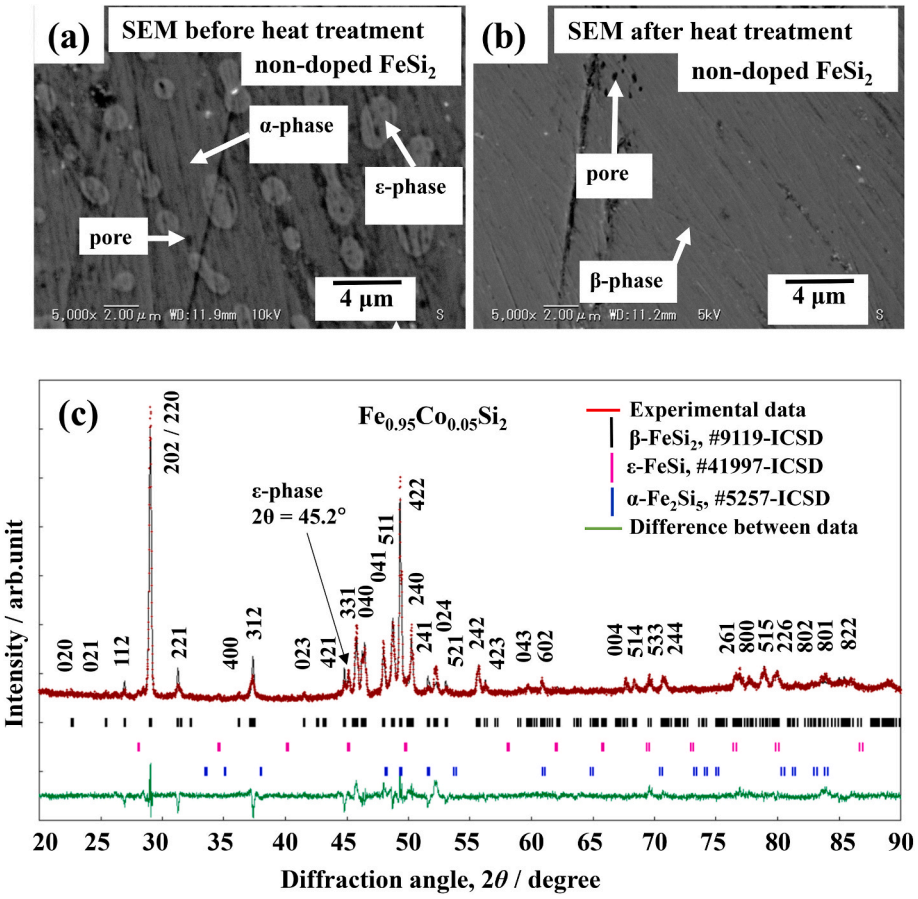

Fig. 2. (a) SEM micrograph of pure $FeSi_2$ before heat treatment and (b) after heat treatment. The arrows indicate the grain of ε, α, β-phase, and pores. (c) Rietveld refinement of 5 % Co-doped $FeSi_2$. The indexed peaks are the peaks of β-phase and the arrow shows the trace of ε-phase on the right of (421)-plane. The highest intensity is obtained at (202)/(220)-plane.

Fig. 2(a)–(b). Before heat treatment, there is a grain of ε-phase (bright) and α-phase (dark). After heat treatment at 1423 K for 3 h and followed by 1113 K for 20 h, the microstructure became homogeneous, indicating the formation of semiconducting β-phase. This tendency agrees with the report of Dabrowski et al. [24]. In addition, as shown in Fig. S3 in Supporting Information, after heat treatment, the surface morphology of all samples ($0 \leq x \leq 0.05$) is homogeneous, indicating only semiconducting β-phase. No secondary phase is observed for all heat-treated samples. However, according to Rietveld's refinement results from Table S1 in Supporting Information, the semiconducting β-phase of the non-doped sample (96.98 %) is slightly higher than that of Co-doped samples (~90 %, suggesting that the addition of Co causes the formation of a secondary metallic phase (ε-FeSi and α-Fe_2Si_5). However, the amount of semiconducting β-phase could be maintained higher than 90 % for all samples. The pore is formed because of the fast cooling from the copper heart in the arc melting process and pore size is enlarged after the heat treatment when the volume β-$FeSi_2$ differs from metallic ε-FeSi and α-Fe_2Si_5. Fig. 2 (c) shows the Rietveld refinement of 5 % Co-doped β-$FeSi_2$. It shows a goodness of fitting in the β-phase with the trace of the ε-phase on the right side of the indexed peak (421). In Table S1 of Supporting Information, the reliability factor for all samples of the weighted diffraction pattern R_{wp} is 3.043 % < R_{wp} < 3.268 %, and the index $S = R_{wp}/R_e$ representing a comparison with R_e corresponding to the statistically expected minimum R_{wp} is $3.988 < S < 4.171$. This suggests that goodness of fitting is obtained. The highest intensity is observed at (202/220)-plane. The highest intensity is useful for analyzing the crystalline quality [30]. Therefore, we further use this plane for evaluating the crystallite size and micro-strain.

Fig. 3 (a) shows the tendency full width at half maximum (FWHM, β) and the change in diffraction angle (θ) dependence with Co doping (x). The β values are obtained as $\sqrt{\beta_{exp}^2 - \beta_i^2}$, where β_{exp} is the FWHM of samples $0 \leq x \leq 0.05$ and $\beta_i = 0.079°$ is the diffraction X-ray broadening by the instrument (SmartLab, RIGAKU) [31]. The β values tend to decrease with increasing x, indicating that the quality of $FeSi_2$ becomes degraded when Co is introduced to the based material. In addition, the θ value decreases with x (i.e. the diffraction angle is shifted to the left (smaller value), indicating that the tensile strain happens in the system [32]. Compared to the non-doped sample, it is clear from Fig. 3 (b) that the peak at the (202)/(220) plane of Co-doped samples shifts to the left side (smaller θ values). In general, tensile strain increases the molecular bond length and decreases the force constant, reducing the vibration frequency and shifting the diffraction angle to a smaller value. In contrast, compressive strain shifts the diffraction angle to a higher value. The increase in tensile strain leads to a decrease in lattice thermal conductivity. We then investigate the crystallite sizes and micro-strain. Scherrer's formula can be used to evaluate crystallite size (D) as the following equation [33]:

$$D = \frac{K\lambda}{\beta \cos\theta} \tag{4}$$

The assumption is that Scherrer's constant (K) is 0.9, which means that the crystallite is cubic in shape with a side length of D and the shape of the X-ray diffraction peak is approximated by a Gaussian function [31]. The λ is the X-ray wavelength of Cu K-α having a value of 1.5418 Å. The β is the true FWHM in radian (rad), and θ is the diffraction angle at the (202) or (220) plane. Previous report also used FWHM at this (202)/(220) plane, because this plane has the maximum intensity [30].

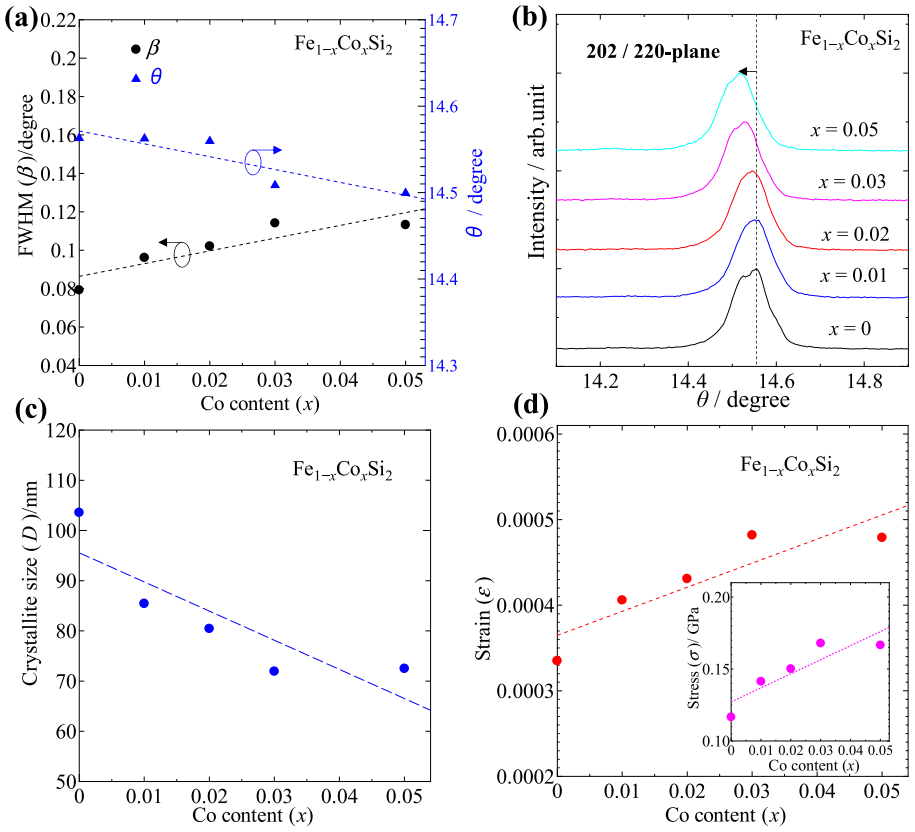

Fig. 3. (a) Full width at half maximum (FWHM, β) and diffraction angle (θ) with x dependence. (b) The peak intensity at 202/220-plane, where the dash straight line and arrow is a guide showing the transition of the peak shifting to the left due to tensile strain. (c) Crystallite size (D) and (d) micro-strain (ε) with x dependence. The inset plots the data of stress (σ).

Therefore, we can obtain the FWHM from the Rietveld analysis. By using **Equation (4)**, the D values with Co doping dependence can be obtained and the data are plotted in Fig. 3 (c). The crystallite size decreases from ~103.57 nm to ~72.49 nm with increasing x. The crystallite size of our sample is slightly bigger than that prepared by the spark plasma sintering method (~50 nm) as reported by Abbassi et al. [19]. However, we could see from the current study that the decrease in crystallite size could also be the reason for thermal conductivity reduction. More grain boundaries are probably formed, resulting in increasing phonon scattering and reducing phonon mean free path. In addition, The relationship between micro-strain (ε), FWHM(β), and θ can be expressed by the following formula [34]:

$$\varepsilon = \frac{\beta \cos\theta}{4} \tag{5}$$

In addition, micro-stress (σ) can be then calculated by Ref. [35]:

$$\sigma = E\varepsilon \tag{6}$$

Where the ε can be obtained from **Equation (2)** and E is Young's modulus having values of 348.4 GPa [36]. Therefore, we can evaluate ε and σ from **Equations (5) and (6)**. In Fig. 3 (d), the micro-strain (ε) increases from ~0.00033 to ~0.00047 with increasing Co doping. As the ε increases, the micro-stress (σ) also increases because of their proportionality. As shown in the inset of Fig. 3(d), The σ increases from ~0.11 GPa to ~0.16 GPa as x increases from 0 to 0.05. We have proven our consideration above that the lattice thermal conductivity of the $FeSi_2$ system decreases due to the increase in internal strain/stress of the system while Co occupies the host $FeSi_2$. The lattice thermal conductivity is characterized by Ref. [37]:

$$\kappa_L = (1/3)C_v\nu_g^2\tau = (1/3)C_v\nu_g l \tag{7}$$

where C_v is the specific heat at constant volume, ν_g is phonon group velocity, τ is relaxation time, and l is phonon mean free path. As

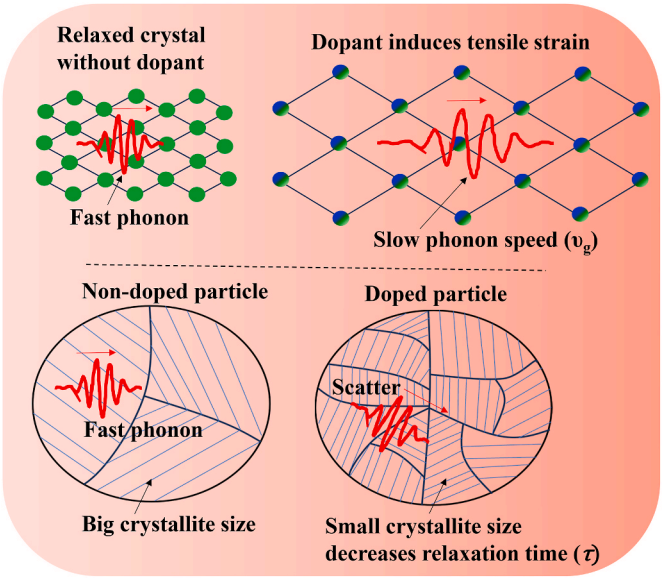

Fig. 4. Schematic illustration of Co dopant induced the tensile strain to the β-$FeSi_2$ system, leading to lattice softening (top) and the crystallite size decrease, leading to phonon scattering (bottom). The lattice softening decreases the phonon velocity while the small crystallite size decreases phonon relaxation time. Both lattice softening and phonon scattering contribute to the reduction in thermal conductivity.

illustrated in Fig. 4, the dopant Co induces the tensile strain and decreases the crystallite size. As a result, the phonon velocity becomes slower, and the relaxation time is smaller due to lattice softening and phonon scattering, respectively.

The lattice softening causes a reduction in phonon velocity because it weakens the bonds between atoms, making the lattice less rigid. Phonon vibrations which usually carry heat, travel faster in a stiffer lattice. When the lattice softens, these vibrations slow down due to decreased stiffness and lower vibrational frequencies. Since phonon velocity is important for heat transfer, a reduction in velocity results in lower thermal conductivity. Thus, softer lattices cause more phonon scattering and decrease the efficient movement of heat through the material.

The small crystallite sizes form more grain boundaries that act as barriers to phonon transport, leading to a reduction in phonon relaxation time (the average time between phonon collisions). Shorter relaxation times increase phonon scattering, reducing the efficiency of heat transfer and consequently decreasing thermal conductivity. In thermoelectric application, it is important that smaller crystallites create more barriers in the phonon path, leading to a reduction in thermal conductivity.

4. Conclusion

In summary, we found that the Co doing increases the tensile strain of β-$FeSi_2$ crystal. In addition, the Co substitution also decreases the crystallite size of the host crystal. The increase of tensile strain and decrease in crystallite size lead to lattice softening and phonon scattering, indicating the origin of the reduction of thermal conductivity. This study could be beneficial for understanding the correlation between thermal transport and crystal properties of metal silicides.

CRediT authorship contribution statement

Sopheap Sam: Writing – review & editing, Writing – original draft, Visualization, Validation, Methodology, Investigation, Formal analysis, Data curation, Conceptualization. **Kosuke Yamazaki:** Data curation. **Hiroshi Nakatsugawa:** Supervision, Software, Resources, Project administration, Funding acquisition.

Declaration of competing interest

The authors declare that they have no known competing financial interests or personal relationships that could have appeared to influence the work reported in this paper.

Data availability

Data will be made available on request.

Acknowledgments

The XRD and SEM-EDS measurements were performed at the Instrumental Analysis and Evaluation Center, Yokohama National University. The thermal conductivity was measured by the PEM-2 apparatus at National Defense Academy.

Appendix A. Supplementary data

Supplementary data to this article can be found online at https://doi.org/10.1016/j.ssc.2024.115700.

References

[1] X.-L. Shi, J. Zou, Z.-G. Chen, Chem. Rev. 120 (2020) 7399–7515, https://doi.org/10.1021/acs.chemrev.0c00026.
[2] S. Sam, L.A. Gan Lim, S. Thirumalai, A. Wiranata, Jamasri, J. Sentanuhady, G.N. C. Santos, M.A. Muflikhun, Manuf. Lett. 40 (2024) 11–15, https://doi.org/10.1016/j.mfglet.2024.01.002.
[3] H.J. Goldsmid, Theory of thermoelectric refrigeration and generation, in: H. Robert, J. Chennupati, K. Yoshiyuki, M.O. Richard, P. Jürgen, S. Tae-Yeon, U. Shin-ichi, M.W. Zhiming (Eds.), Intoduction to Thermoelectr, second ed., Springer Berlin Heidelberg, Berlin, Heidelberg, 2016, pp. 9–24, https://doi.org/10.1007/978-3-662-49256-7_2.
[4] M. Nomura, R. Anufriev, Z. Zhang, J. Maire, Y. Guo, R. Yanagisawa, S. Volz, Mater. Today Phys. 22 (2022) 100613, https://doi.org/10.1016/j.mtphys.2022.100613.
[5] N. Liu, S.E. Rezaei, W.A. Jensen, S. Song, Z. Ren, K. Esfarjani, M. Zebarjadi, J. A. Floro, Adv. Funct. Mater. 29 (2019) 1903157, https://doi.org/10.1002/adfm.201903157.
[6] X. Du, P. Hu, T. Mao, Q. Song, P. Qiu, X. Shi, L. Chen, ACS Appl. Mater. Interfaces 11 (2019) 32151–32158, https://doi.org/10.1021/acsami.9b10648.
[7] S. Sam, U. Farooq, M. Namba, K. Yamazaki, H. Nakatsugawa, J. Alloys Compd. 989 (2024) 174367, https://doi.org/10.1016/j.jallcom.2024.174367.
[8] S. Sam, U. Farooq, R. Oshita, H. Nakatsugawa, J. Phys. Chem. Solids 194 (2024) 112224, https://doi.org/10.1016/j.jpcs.2024.112224.
[9] P. Qiu, J. Cheng, J. Chai, X. Du, X. Xia, C. Ming, C. Zhu, J. Yang, Y. Sun, F. Xu, X. Shi, L. Chen, Adv. Energy Mater. 12 (2022) 2200247, https://doi.org/10.1002/aenm.202200247.
[10] S. Sam, H. Nakatsugawa, Y. Okamoto, Mater. Adv. 4 (2023) 2821–2830, https://doi.org/10.1039/D3MA00153A.
[11] S. Sam, S. Odagawa, H. Nakatsugawa, Y. Okamoto, Materials 16 (2023) 927, https://doi.org/10.3390/ma16030927.
[12] X. Du, P. Qiu, J. Chai, T. Mao, P. Hu, J. Yang, Y.-Y. Sun, X. Shi, L. Chen, ACS Appl. Mater. Interfaces 12 (2020) 12901–12909, https://doi.org/10.1021/acsami.0c00321.
[13] S. Sam, H. Nakatsugawa, Y. Okamoto, Jpn. J. Appl. Phys. 61 (2022) 111002, https://doi.org/10.35848/1347-4065/ac96b7.
[14] J. Cheng, L. Gan, J. Zhang, J. Xi, L. Xi, J. Yang, T. Deng, P. Qiu, X. Shi, L. Chen, J. Mater. Sci. Technol. 187 (2024) 248–257, https://doi.org/10.1016/j.jmst.2023.11.039.
[15] S. Sam, K. Yamazaki, H. Nakatsugawa, Solid State Commun. 371 (2023) 115287, https://doi.org/10.1016/j.ssc.2023.115287.
[16] S. Le Tonquesse, Z. Verastegui, H. Huynh, V. Dorcet, Q. Guo, V. Demange, C. Prestipino, D. Berthebaud, T. Mori, M. Pasturel, ACS Appl. Energy Mater. 2 (2019) 8525–8534, https://doi.org/10.1021/acsaem.9b01426.
[17] R. Hanus, M.T. Agne, A.J.E. Rettie, Z. Chen, G. Tan, D.Y. Chung, M.G. Kanatzidis, Y. Pei, P.W. Voorhees, G.J. Snyder, Adv. Mater. 31 (2019) 1900108, https://doi.org/10.1002/adma.201900108.
[18] X. Ai, B. Lei, M.O. Cichocka, L. Giebeler, R.B. Villoro, S. Zhang, C. Scheu, N. Pérez, Q. Zhang, A. Sotnikov, D.J. Singh, K. Nielsch, R. He, Adv. Funct. Mater. 33 (2023), https://doi.org/10.1002/adfm.202305582.
[19] L. Abbassi, D. Mesguich, D. Berthebaud, S. Le Tonquesse, B. Srinivasan, T. Mori, L. Coulomb, G. Chevallier, C. Estournès, E. Flahaut, R. Viennois, M. Beaudhuin, Nanomaterials 11 (2021) 2852, https://doi.org/10.3390/nano11112852.
[20] J. Tani, H. Kido, Jpn. J. Appl. Phys. 40 (2001) 3236, https://doi.org/10.1143/JJAP.40.3236.
[21] O. Yamashita, S. Tomiyoshi, N. Sadatomi, J. Mater. Sci. 38 (2003) 1623–1629, https://doi.org/10.1023/A:1023251004461.
[22] T. Watanabe, M. Hasaka, T. Morimura, H. Nakashima, J. Alloys Compd. 417 (2006) 241–244, https://doi.org/10.1016/j.jallcom.2005.08.067.
[23] Z. He, D. Platzek, C. Stiewe, H. Chen, G. Karpinski, E. Müller, J. Alloys Compd. 438 (2007) 303–309, https://doi.org/10.1016/j.jallcom.2006.08.045.
[24] F. Dąbrowski, Ł. Ciupiński, J. Zdunek, J. Kruszewski, R. Zybała, A. Michalski, K. Jan Kurzydłowski, Mater. Today Proc. 8 (2019) 531–539, https://doi.org/10.1016/j.matpr.2019.02.050.
[25] M. Ohtaki, D. Ogura, K. Eguchi, H. Arai, Chem. Lett. 22 (1993) 1067–1070, https://doi.org/10.1246/cl.1993.1067.
[26] G. Li, W. Bai, N. Shi, Q. Fang, M. Xiong, J. Yang, Z. Ma, H. Rong, Eur. J. Mineral 24 (2012) 1047–1052, https://doi.org/10.1127/0935-1221/2012/0024-2237.
[27] B.C. Sales, E.C. Jones, B.C. Chakoumakos, J.A. Fernandez-Baca, H.E. Harmon, J. W. Sharp, E.H. Volckmann, Phys. Rev. B 50 (1994) 8207–8213, https://doi.org/10.1103/PhysRevB.50.8207.
[28] Y. Dusausoy, J. Protas, R. Wandji, B. Roques, Acta Crystallogr. Sect. B Struct. Crystallogr. Cryst. Chem. 27 (1971) 1209–1218, https://doi.org/10.1107/S0567740871003765.
[29] L.-D. Zhao, S.-H. Lo, J. He, H. Li, K. Biswas, J. Androulakis, C.-I. Wu, T.P. Hogan, D.-Y. Chung, V.P. Dravid, M.G. Kanatzidis, J. Am. Chem. Soc. 133 (2011) 20476–20487, https://doi.org/10.1021/ja208658w.
[30] K. Watanabe, T. Taniguchi, S. Sakane, S. Aoki, T. Suzuki, T. Fujita, Y. Nakamura, Jpn. J. Appl. Phys. 56 (2017) 05DC04, https://doi.org/10.7567/JJAP.56.05DC04.
[31] H.P. Klug, L.E. Alexander, X-Ray Diffraction Procedure, John Wiley &Sons Inc., New York, 1954, pp. 491–538.
[32] A. Yuan, H. Zhang, Q. Deng, Molecules 24 (2019) 3662, https://doi.org/10.3390/molecules24203662.
[33] P.P. Hankare, P.A. Chate, M.R. Asabe, S.D. Delekar, I.S. Mulla, K.M. Garadkar, J. Mater. Sci. Mater. Electron. 17 (2006) 1055–1063, https://doi.org/10.1007/s10854-006-9034-2.
[34] P.P. Hankare, P.A. Chate, D.J. Sathe, P.A. Chavan, V.M. Bhuse, J. Mater. Sci. Mater. Electron. 20 (2009) 374–379, https://doi.org/10.1007/s10854-008-9736-8.

[35] G.A. Jeffery, J. Chem. Educ. 34 (1957) A178, https://doi.org/10.1021/ed034pA178.
[36] G.-M. Wang, W. Zeng, X. Xu, W.-H. Liu, B. Tang, D.-H. Fan, Q.-J. Liu, X.-H. Chang, M. Zhong, Phys. Status Solidi 257 (2020) 1–9, https://doi.org/10.1002/pssb.202000083.
[37] T. Takeuchi, New thermoelectric materials with precisely determined electronic structure and phonon dispersion, in: D.M. Rowe (Ed.), Thermoelectr. Its Energy Harvest., first ed., Taylor & Francis Group, Abingdon, UK, 2017 https://doi.org/10.1201/b11891, 7-1-7–27.